

SCIENTIFIC REPORTS

OPEN

Dynamic control of particle separation in deterministic lateral displacement separator with viscoelastic fluids

Yuke Li¹, Hongna Zhang^{1,2}, Yongyao Li¹, Xiaobin Li², Jian Wu¹, Shizhi Qian³ & Fengchen Li²

We proposed an innovative method to achieve dynamic control of particle separation by employing viscoelastic fluids in deterministic lateral displacement (DLD) arrays. The effects of shear-thinning and elasticity of working fluids on the critical separation size in DLD arrays are investigated. It is observed that each effect can lead to the variation of the critical separation size by approximately 40%. Since the elasticity strength of the fluid is related to the shear rate, the dynamic control can for the first time be easily realized through tuning the flow rate in microchannels.

A deterministic lateral displacement (DLD) array is a microfluidic particle-separation device that takes advantage of the asymmetric bifurcation of laminar flow around obstacles, which was firstly introduced by Huang *et al.*¹ Since the invention of DLD, diverse applications have been realized in sorting and enrichment in tumor research and clinical diagnostics, e.g. purification of *Aspergillus* spores², blood analysis^{3–5}, detection of circulating tumor cells^{6–8}, where DLD arrays are used to separate particles or cells by size from millimeter to sub-micrometer.

The DLD devices comprise a periodic array of micrometer-scale obstacles, which decides the separation distance of the particles with different sizes, as shown in Fig. 1(a). In a DLD device, the gap distance between two lateral posts is D_x and the distance along the flow direction between the nearest posts of adjacent rows is D_y , as shown in Fig. 1(b). The basic principle can be understood by the streamline orientation of DLD arrays. Fluid emerging from the gap between two posts will encounter another post in the next row, and therefore it will bifurcate as it moves around the post. After negotiating N (a period) obstacles, the fluid can conceptually be divided into N regions. When a small particle enters the array and negotiates the posts, it will follow streams continuously, and after encountering N posts i.e. N rows, it will restore to the original direction, moving in an average flow direction matching the fluid. This particle motion is termed as “zigzag mode” (see Fig. 1(c) and Supplementary Video S1). However, a larger particle whose center is out of the boundary of the first stream will be displaced laterally by the obstacles into the second stream. This motion is termed as “displacement mode” (see Fig. 1(d) and Supplementary Video S2). By accumulating the cross-flow displacement, the larger particle will eventually migrate across the streamlines with the direction θ . The transition between two modes is sharp and it occurs at a critical size D_c , about twice width of the first stream. The principle of the critical particle size implies that the particle motion in a fixed DLD array is bimodal either with diameter lower than D_c in “zigzag mode” or with diameter larger than D_c in “displacement mode”. Since each stream carries the same fluid flow, D_c can be analytically approximated using⁹, $D_c = 2\alpha D_x/N$, where α is a variable parameter to accommodate for non-uniform flow through the gap. Davis¹⁰ derived a power-law formula ($D_c = 1.4D_xN^{-0.48}$) to predict D_c by fitting the data collected over about 20 different devices over a wide range of D_x from 1.3 μm to 38 μm and N from 2 to 20.

The bimodal separation however cannot meet the need for practical applications, in which suspensions with particles of various sizes are required to operate. To this end, various advanced DLD devices were designed for multiple critical thresholds, and the corresponding methods can be regarded as passive ones and active ones. A passive DLD device with multiple critical sizes utilizes the adjustment of the configuration of posts, e.g. the shape of posts¹¹, the depth of the channel¹², the gap between the posts¹³, and hydrodynamic forces¹⁴, and so on. An active DLD, however, enable to tune critical diameters with external forces exerted on particles and even a live

¹School of Energy Science and Engineering, Harbin Institute of Technology, Harbin, 150001, China. ²Sino-French Institute of Nuclear Engineering and Technology, Sun Yat-sen University, Zhuhai, 519000, China. ³Institute of Micro/Nanotechnology, Old Dominion University, Norfolk, Virginia, 23529, USA. Correspondence and requests for materials should be addressed to H.Z. (email: zhanghn@hit.edu.cn) or F.L. (email: lifch6@mail.sysu.edu.cn)

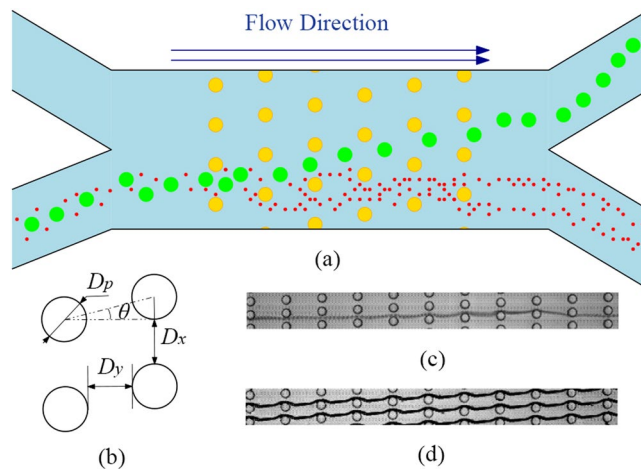


Figure 1. Schematics of (a) a DLD device with periodic arrays (yellow) and how large particles (green) and small particles (red) are separated, (b) a unit of rhombic posts with diameter D_p , Superposition photos of particles behaving (c) *zigzag mode* ($N=8$), (d) *displacement mode* ($N=8$).

feedback setup can be realized. Several active technologies have been proposed, e.g. mechanical¹⁵, gravitational¹⁶, dielectrophoretic (DEP)^{17,18} and acoustic¹⁹, and so on.

In recent years, viscoelastic-based particle separation^{20–24} and focusing^{25–29} have been known as an efficient way to manipulate particles in microfluidics. By adding only small amount of synthetic polymers or biological polymers, such as DNA and hyaluronic acid, center-focusing in non-Newtonian fluids provides a new approach to manipulate different particles, including blood cells^{20,21,23}, magnetic particles^{27,28}, even nano-particles²². The normal stresses arising from fluid viscoelasticity are responsible for particle lateral migration to the narrow central core region of the channel in elasticity-dominant fluid^{30–32}. The elastic lift force F_e scaling as $F_e \propto a^3 \nabla N_1$ ³³ (the first normal stress difference $N_1 = \tau_{11} - \tau_{22}$, where subscripts 1 and 2 are the direction of primary velocity and the direction of velocity variation, respectively) in inertial microfluidics suggests particle migration velocity is strongly dependent on blockage ratio and viscoelasticity of the fluid medium³⁴. Inspired by F_e pushing particles away from sidewalls, particles may suffer extra repulsive elastic force on particles when they passing through periodic obstacles in DLD arrays. We introduced viscoelasticity of fluid medium into DLD arrays to observe peculiar phenomenon.

In this paper, we realize dynamic control of D_c in DLD separators by introducing viscoelastic fluids. This is for the first time to adopt viscoelastic fluids in DLD, while all previous papers are restricted to Newtonian fluids, except one to shear-thinning effects numerically¹⁴. One most important advantage of this technology is offering considerable control of D_c in a single DLD device. The peculiar rheological properties of non-Newtonian liquids, such as non-zero normal stress differences, shear-rate-dependent viscosity³⁵, etc., can be exploited to design spectacular devices or improve some existing processes. Therefore, in DLD devices, the introduction of shear-rate-dependent viscosity and nonlinear elastic forces is expected to modify the critical particle size D_c . Comparing with other active DLD devices, an obvious advantage of employing non-Newtonian fluids in DLD devices is that other auxiliary equipment is no longer required. D’Avino¹⁴ mainly focused on the shear-thinning fluid and observed that D_c declines with shear-thinning effect enhanced numerically. Here, not only shear-thinning but also elastic effects of the applied viscoelastic fluid medium on particle separation in a DLD device are performed through extensive experimental investigations. We further realize a dynamic variation of D_c by altering the flow rate utilizing the elasticity.

Results

Table 1 presents the rheology information of test fluids. Aqueous Xanthan solutions are strongly shear-thinning fluid (see Fig. 2(a)) without significant normal stress difference observed³⁶ and PVP solutions has a constant viscosity at a certain concentration but with elasticity (see Fig. 2(b,c)). This helps us to isolate the effects of shear-thinning and elasticity of non-Newtonian fluid medium. Xanthan Gum solutions were modeled by power-law fluid and each power law index n indicates a different concentration of Xanthan Gum solution. PVP solutions are Boger type, with constant viscosity (η) during decades of shear rate, and its remarkable elasticity is characterized by relaxation time (λ). Figure 3 illustrates the dynamic range of D_c of DLD devices with $N=5$ and 8 for different fluids. Although displacement angle φ for *displacement mode* is θ , there remains displacement angle φ ($0 < \varphi < \theta$) where particles don’t either behave *zigzag mode*. However, the geometry parameters chosen here ($D_y/D_x = 10/3$) guarantees the symmetry of the flow lane distribution and meanwhile avoids “mixed motion”, i.e., particle trajectory with a displacement angle φ ($0 < \varphi < \theta$)³⁷. Moreover, the intermediary angle is short in this paper and have little influence on particle separation in DLD. It is also unrealistic to separate particles with similar size by hydrodynamic forces. We hence note that particles whose displacement angle is over zero have entered *displacement mode*. After superposition of over 10,000 images captured by the camera via Z Project in ImageJ, examples of which can be seen in Fig. 1(c,d), the mode of particles entering a certain mode are determined, either

Solutions	Concentration	Power law fit ($\eta = m\dot{\gamma}^{n-1}$)		$\eta(\text{Pa}\cdot\text{s})$	$\lambda(\text{s})$
		m	n		
Xanthan gum	700 ppm	0.090	0.685		
	1000 ppm	0.149	0.608		
	1500 ppm	0.359	0.526		
PVP	3000 ppm			0.155	2.15×10^{-3}
PVP	8000 ppm			0.385	2.57×10^{-3}

Table 1. Rheology information of test fluids: power law fitting parameter of viscosity versus shear rate of Xanthan Gum solution, and constant viscosities and relaxation times of PVP solutions as a Boger fluid.

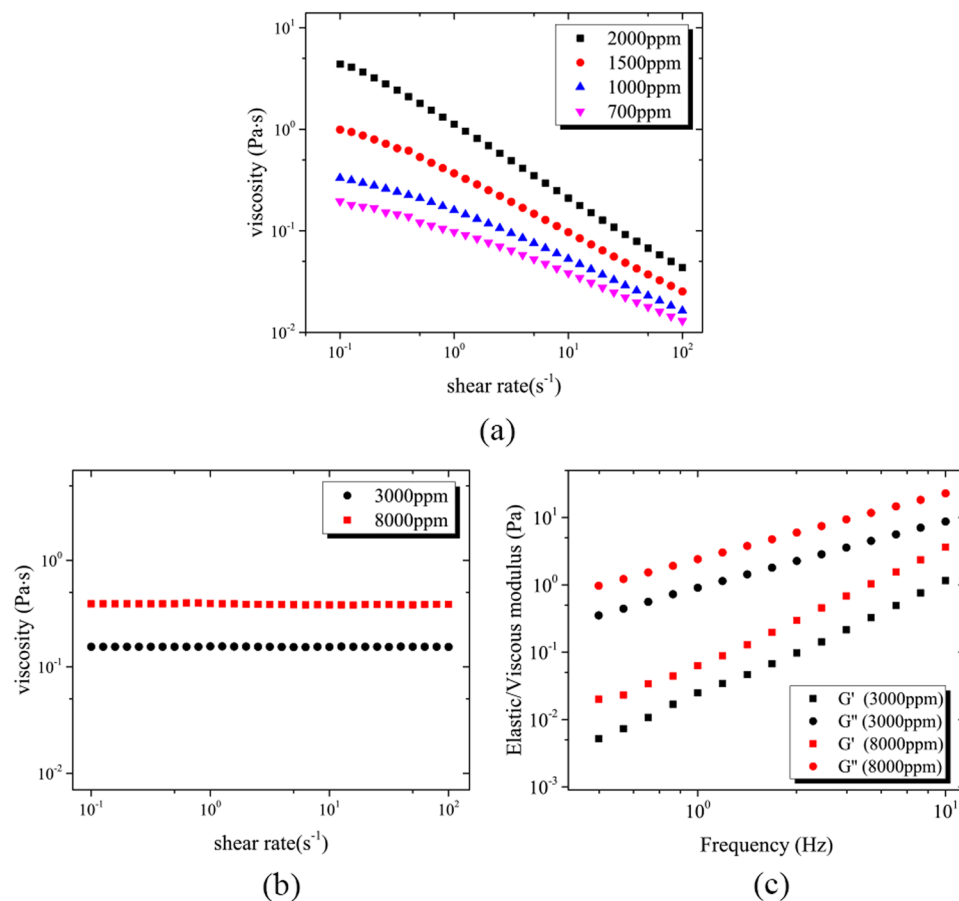


Figure 2. (a) Viscosity versus shear rate of Xanthan Gum solutions with different concentrations. (b) Viscosity versus shear rate and (c) elastic/viscous modulus versus frequency of PVP solutions with different concentrations.

zigzag or *displacement*. The modes of particle in different circumstances including particle diameter, N , n , and Wi were plotted.

In order to illustrate the dynamic control of particle separation in viscoelastic DLD devices, we present the separation of particles with diameter $8\ \mu\text{m}$ and $12\ \mu\text{m}$ in Fig. 4 and Supplementary Video S3. At first, both $8\text{-}\mu\text{m}$ and $12\text{-}\mu\text{m}$ particles behave *zigzag* mode at $Wi = 0.1$, i.e., low flow rate. The critical size at this situation is around $13\ \mu\text{m}$. With the flow rate gradually increasing, D_c declines due to the increased Wi . $12\text{-}\mu\text{m}$ particles enter *displacement* mode once D_c decreases under $12\ \mu\text{m}$ while $8\text{-}\mu\text{m}$ particles remain unchanged since D_c is still over $8\ \mu\text{m}$ at approximately $Wi = 0.5$. At this situation, we realize separation of particles with two diameters by tuning flow rate despite that they cannot be separated in Newtonian DLD devices with the same geometry and flow rate. With the flow rate further increasing, both $8\text{-}\mu\text{m}$ and $12\text{-}\mu\text{m}$ particles enter *diplacement* mode presented as Fig. 4(c).

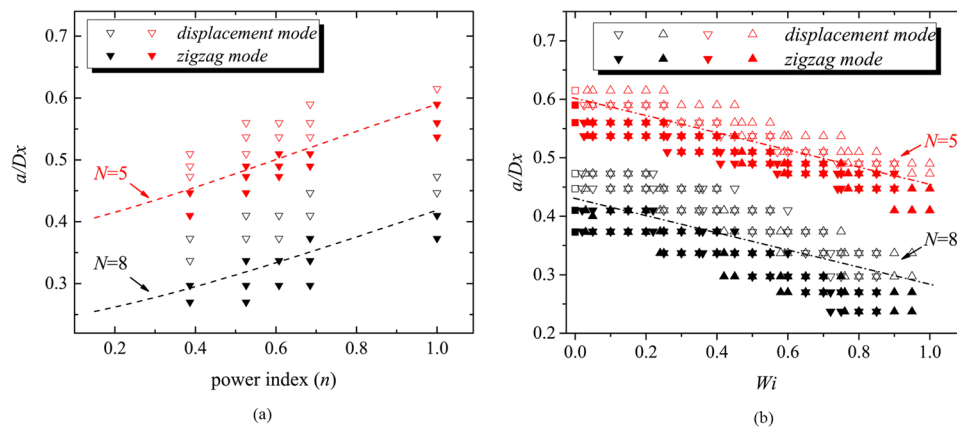


Figure 3. Dimensionless a/D_x versus (a) power index n and (b) Weissenberg number Wi , where a is the particle diameter. The diameters of particles adopted in this experiments are listed in Table 2. (a) The dashed lines are results predicted by numerical simulation¹⁴. The formula to calculate D_c is described as $D_c/D_x = f(n)/(f(n) + N - 2)$, where $f(n) = 1.86 + 1.08n + 1.38n^2$ ¹⁴. (b) All solid triangles are particles behaving zigzag mode, while hollow ones displacement mode; downward ones in 3000 ppm PVP solutions, while upward ones in 8000 ppm PVP solutions; red ones in $N = 5$, while black ones in $N = 8$.

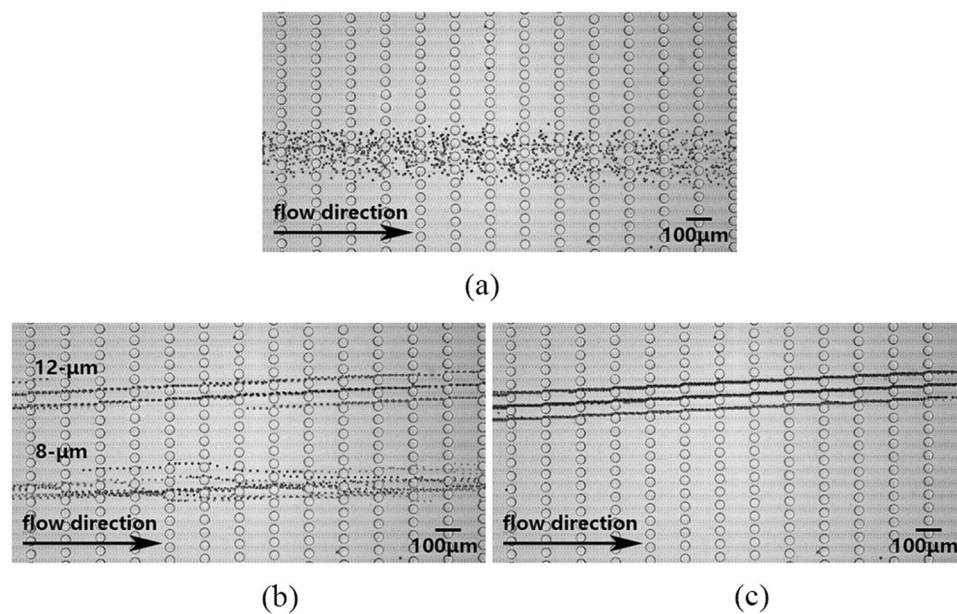


Figure 4. Dynamic control of particle separation in viscoelastic DLD via flow rate at (a) $Wi = 0.1$, (b) $Wi = 0.5$, and (c) $Wi = 0.9$. (a) Particles with diameter $8 \mu\text{m}$ and $12 \mu\text{m}$ behave zigzag mode at low Wi , i.e., low flow rate; (b) $12 \mu\text{m}$ particles enter displacement mode while $8 \mu\text{m}$ particles remain unchanged when the flow rate gradually increases; (c) Both $12 \mu\text{m}$ and $8 \mu\text{m}$ particles finally enter displacement mode over a critical flow rate. In this way, D_c can be tuned by flow rate in viscoelastic DLD. The images are superposed over the Supplementary Video S3.

Particle diameter a (μm)	7.1	8.2	8.9	10.1	11.2	12.3	13.4
Error bar (μ)	± 0.28	± 0.23	± 0.22	± 0.19	± 0.19	± 0.20	± 0.21
Particle diameter a (μm)	14.2	14.695	15.3	16.1	16.8	17.8	18.9
Error bar (μ)	± 0.19	± 0.15	± 0.14	± 0.15	± 0.14	± 0.15	± 0.16

Table 2. The diameters of particles with error bars adopted in this experiments.

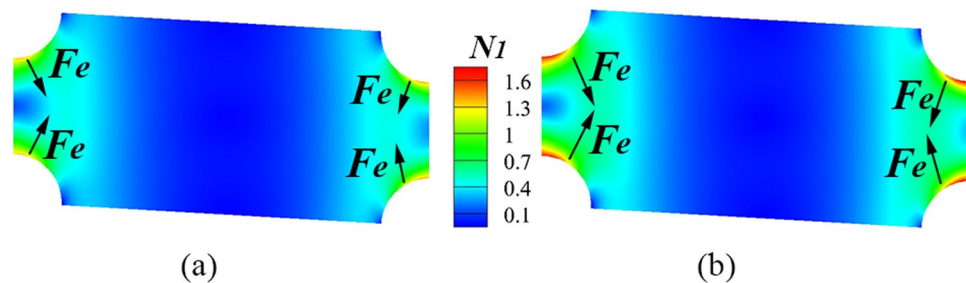


Figure 5. Contour of N_1 over a unit of a DLD array at (a) $Wi = 0.2$ and (b) $Wi = 10$. The arrows represent the direction of elastic force F_e .

Discussion

The separation threshold versus shear-thinning effect is presented in Fig. 3(a). It is observed that D_c declines with n decreasing, which implies that we can separate particles with different critical sizes in one exact DLD device, by only changing the shear-thinning fluid medium with different concentrations. The experimental results are basically in consistence with the dashed lines that were provided by D'Avino¹⁴ with numerical results.

The basic principle of particle separation in DLD can be understood by the streamline orientation of DLD arrays. Fluid emerging from a gap between two obstacles will encounter another one in the next row and will bifurcate as it moves around the obstacle. As this process repeats, periodical bifurcation of the fluid results in the N regions returning to their original relative position with the single gap. Each region entrains the same amount of fluid with the others and carries the same group of molecules following the same path throughout the array. Therefore, David *et al.*⁹ derived a formula $D_c = 2\alpha D_x / N$ to calculate theoretical D_c . In this formula, parameter α denotes the non-uniformity of the flow through the gap. If the fluid flow velocity profile between the two posts is plug-like, $\alpha = 1$; if the flow velocity profile is parabolic, $\alpha = \sqrt{N/3}$ demonstrated by Beech³⁸, considering practical reality. Fluid flow with different shear-thinning effect corresponds to a different α , and consequently D_c . The modification of D_c in shear-thinning fluids is due to that the shear-thinning effect flats the parabolic velocity profile between the posts nearby and thus the width of the outermost flow lane, become larger than that in Newtonian fluids¹⁴. The thinner the shear of the fluid is, the smaller α is. In our experiments, the maximum value of the relative difference of D_c with power-law and Newtonian fluids is found to be around 40% (i.e., when $N = 8$, $D_c \approx 12.3 \mu\text{m}$ in Newtonian fluids, whereas $D_c \approx 7.1 \mu\text{m}$ in a 2000 ppm Xanthan solution). Note that changing the fluid medium still seems to be complicated to alter D_c in a single DLD device.

We then employ PVP solutions as our testing fluids. As PVP solutions behave like a Boger fluid³⁹, they allow us to investigate the elastic effects of viscoelastic fluids solely. Figure 3(b) illustrates the motion modes of particles with different sizes under different Weissenberg number ($Wi = \lambda u / D_x$, where u is average velocity when the fluid flows through the gap between neighbor posts, and in the limiting case, Wi in the Newtonian case is regarded as zero). Considering that each inlet has the same area of the cross section and flow rate, u is obtained by dividing the flow rate by the area of the cross section between two posts to calculate Wi . The Wi number indicates the strength of elastic effect on the flow, and it is in a positive linear relationship with the flow rate. It is clear that, in the two DLD arrays with $N = 5$ and 8 , D_c in PVP solutions becomes smaller than that in Newtonian fluids. And D_c decreases along with the increase of Wi . The fit between D_c and Wi seems to be linear for the same N (the dashed line nipped by *displacement* and *zigzag mode* in Fig. 3(b)). The above finding implies that although both the DLD array and the fluid medium are fixed, we can still tune D_c of a DLD device by changing Wi , i.e., the flow rate at the inlet, to achieve dynamic control of particle separation.

In order to explain the abnormal change of D_c with the Boger fluid, we take into account the first normal stress difference of the viscoelastic fluid flow. In a viscoelastic Poiseuille flow, suspended particles will laterally migrate towards specific equilibrium positions due to the non-uniform N_1 and the second normal stress difference N_2 . N_2 is usually neglected because of its relatively small magnitude ($\sim O(10^{-2})$) comparing with N_1 ⁴⁰. The elastic lift force F_e in inertial microfluidics can be expressed as $F_e \propto a^3 \nabla N_1$ ³³. The elastic force arising from the non-uniform N_1 plays a more significant role than other inertial lift forces when elasticity is dominant. Especially in a pure elastic flow, particle will migrate towards the centerline in a circular tube and another four corners in a channel with a square cross section, where N_1 is lower than other regions³³. Inspired by the elastic force arising from N_1 in inertial microfluidics, we attribute the decrease of D_c in the Boger fluid to the appearance of non-uniform N_1 . The application of an elastic lift force pushes the particle out from the post into the neighboring lamina, displacing the particle despite that its size is smaller than the critical size in the Newtonian case. Therefore, in a DLD device, the transition from the zigzag motion to the *displacement mode* is advanced by extra elastic force with the particle size getting increased. Numerical simulations of single-phase viscoelastic elastic fluid flow passing through periodic obstacles are simulated to demonstrate the distribution of N_1 . Since particles suffer the periodic forces in every unit, we performed two-dimensional numerical simulations on fluid flow in a unit of DLD array (Fig. 1(b)) via *OpenFOAM*⁴¹.

Figure 5 plots the contour of N_1 in one unit at $Wi = 0.2$ and 10 . The elastic force pushes particles towards lower N_1 region, whose direction are presented along the arrow in Fig. 5. Moreover, the gradient of N_1 , ∇N_1 , at high Wi is greater than that at small Wi , and consequently a large elastic force is exerted on the particle. That's why D_c becomes smaller when Wi increases. It can also be understood by shell model induced by irreversible non-hydrodynamic interactions⁴². The elastic force arising from the non-uniform N_1 enlarge the hard-wall

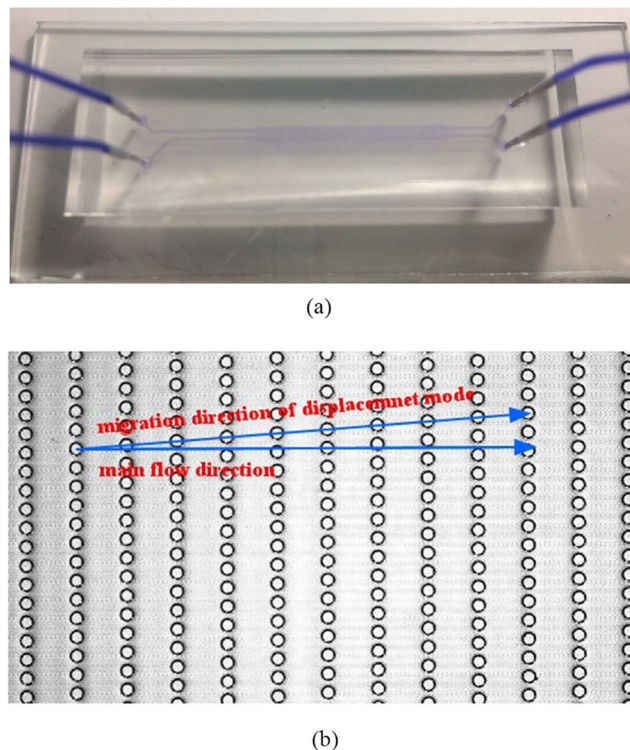


Figure 6. (a) A snapshot of the microfluidic channel with poly(dimethylsiloxane) (PDMS)-glass compounded layer field with purple dye. (b) A grey-scaled image of micro-posts in the microchannel. The direction of main flow and displacement mode are presented.

potential of the model. The current work does not enter the further higher Wi region. For even high Wi , much lower D_c may be allowed. However, the strength of the microchannel cannot meet the demand for higher pressure drop as the viscosity in PVP solutions is 2 order higher than that in Newtonian fluids. It will be valuable to search for a typical elastic fluid with a lower viscosity and strong elasticity in the future.

In summary, we investigated how the critical separation size D_c of the deterministic lateral displacement (DLD) device is influenced by non-Newtonian fluids, i.e., the shear-thinning effect and the elastic effect. For the first time, dynamic control of D_c can be easily realized through only tuning the flow rate in microchannels. Our experimental results show that both the shear-thinning and elastic effects can be used to tune D_c of a DLD array. It is found that D_c decreases when power law index n decreases or Wi increases. The maximum reduction of modified D_c in the experiments with non-Newtonian fluids over D_c in Newtonian fluids is up to 40% approximately. The variation of D_c under shear-thinning effect is attributed to a flatter velocity profile between two neighboring posts. We believe the extra elastic force arising from the non-uniform first normal stress difference N_1 is responsible for the reduction of D_c in elastic fluid medium. Moreover, larger Wi provides larger ∇N_1 between the posts so that D_c declines more rapidly than that at low Wi . In this manner, a new dynamic approach to tuning D_c in a DLD array is proposed: the flow rate of a DLD array can be utilized to tune D_c in viscoelastic fluid medium. In a DLD device, although D_c in Newtonian fluids is fixed, we can change the fluid medium with different shear-thinning strength to alter D_c . Adopting viscoelastic fluid offers a new opportunity of dynamically tuning D_c by changing the flow rate, which can greatly simplify the existing methods of particle separation control in DLD devices without introducing any auxiliary equipment.

Methods

Microchannel Fabrication and Design. The microfluidic channel was fabricated by the soft lithography techniques using poly(dimethylsiloxane) (PDMS)-glass compounded layer, as shown in Fig. 6. Liquid PDMS was prepared by mixing pre-polymer (Sylgard 184, Dow Corning, USA) with the curing agent by the weight ratio of 10:1. Once both liquid components are thoroughly cross-linked and degassed, PDMS was cast over the SU8 (MicroChem, Newton, MA, USA) master mold on a silicon substrate and then was baked in an oven at 80 °C for 1 hour. After the PDMS was peeled off from the channel mold, several holes were punched through the PDMS slab according to the reserved circles in the microchannel serving as reservoirs of inlets and outlets. The PDMS slab was then treated with oxygen plasma (Harrick, USA) and bonded to a glass substrate. The plastic tubes were inserted through these ports and the tubes were sealed at the junction with the PDMS slab using the glue. Finally, the PDMS-glass assemble device was placed into an oven at 80 °C for 30 minutes to enhance the bonding. The geometry parameters chosen here: $N = 5$ or 8, $D_x = 30 \mu\text{m}$, $D_p = 50 \mu\text{m}$ and $D_y = 10/3 \times D_x$, which guarantees the symmetry of the flow lane distribution and meanwhile avoids “mixed motion”³⁷.

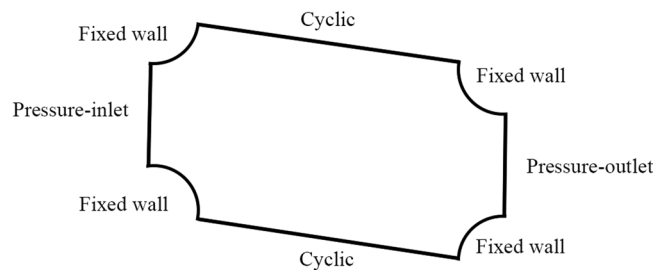


Figure 7. Boundary conditions of a 2-D unit of a DLD array in numerical simulations.

Working Fluids Preparation. The shear-thinning Xanthan solution was prepared by adding Gum Xanthan ($M_w = 4 \times 10^6$ g/mol, Sigma-Aldrich, USA) powder to 22 wt% glycerin (Sigma-Aldrich, USA) aqueous solution (deionized water) to match the density of the polystyrene (PS) particles (1.05×10^3 kg/m³). The viscoelastic Boger fluid³⁹ was prepared by adding polyvinylpyrrolidone (PVP) ($M_w = 3.6 \times 10^5$ g/mol, Sigma-Aldrich, USA) to 22 wt% glycerin (Sigma-Aldrich, USA) aqueous solution. The sample liquid was made by adding polystyrene (PS, Applied Microspheres, the Netherlands) particles into buffer liquid with 0.05%wt Tween 20 (Sigma-Aldrich, USA), which was used to prevent particles' aggregation. All solutions were well stirred for 24 hours and kept for another 24 hours. The volume fraction of particles in the suspension is 0.003. Table 2 presents the particle diameters and their error bars. The viscosity versus shear rate and dynamic oscillation of elastic and viscous modulus was measured by a rotational rheometry (Kinexus, Malvern Instruments Ltd.) equipped with cone-plate geometry (diameter $d = 60$ mm, cone angle $\alpha = 1^\circ$) at $T = 298$ K. The instrument operates in a strain-controlled mode and all frequency sweeps were done at strain amplitudes $\gamma_0 < 100\%$ to assure the linear viscoelastic response regime. The characteristic shear relaxation time λ is calculated from the low frequency part of the data according to $\lambda = \lim_{\omega \rightarrow 0} \frac{G'}{G''\omega}$, where the limiting scaling relations satisfy $G' \sim \omega^2$ and $G'' \sim \omega$.

Experimental Procedures and Image Analysis. Experimental liquids were injected into the microchannels in a 1-mL syringe (Hamilton, Switzerland) with a syringe pump (Harvard, USA). The chip was mounted on the stage of an inverted microscope (IX71, Olympus, Japan), the motion was captured by a high-speed camera (Phantom v.73, Vision Research Inc., USA) with the rate of 100 images per second and the images were analyzed utilizing the ImageJ software (Fiji, ImageJ 1.51 n).

Numerical Method. The simulations were performed using *OpenFOAM* (open source CFD software, *OpenFOAM-extend* 3.2) which is based on Finite Volume Method (FVM)⁴³. The governing equations are made dimensionless by taking the gap D_x as characteristic length, the maximum velocity u_m as characteristic velocity, the viscosity η_0 as characteristic viscosity. Denoting with starred symbols the dimensionless quantities, the fluid flow was simulated in the device by solving the incompressible Navier-Stokes and continuity equations:

$$\frac{\partial \mathbf{u}^*}{\partial t^*} + \mathbf{u}^* \cdot \nabla^* \mathbf{u}^* = -\frac{\nabla^* p^*}{\rho^*} + \nabla^* \cdot \boldsymbol{\tau}^*, \quad \nabla^* \cdot \mathbf{u}^* = 0, \quad (1)$$

where $\boldsymbol{\tau}^*$ is the dimensionless total stress, which can be written split into polymeric (viscoelastic) part separately and the solvent part. Therefore, the momentum balance equations for Oldroyd-B model is

$$\frac{\partial \mathbf{u}^*}{\partial t^*} + \mathbf{u}^* \cdot \nabla^* \mathbf{u}^* = -\frac{\nabla^* p^*}{\rho^*} + \frac{\beta}{Re} \nabla^{*2} \cdot \mathbf{u}^* + \frac{1-\beta}{ReWi} (\nabla^* \cdot (\mathbf{C} - \mathbf{I})), \quad (2)$$

\mathbf{C} is the conformation tensor of polymer molecules or surfactant micelles and Re and Wi are dimensionless numbers defined as $Re = \rho U_m D_x / \eta_0$ and $Wi = \lambda U_m / D_x$, which represent inertial forces versus viscous forces and elastic forces versus viscous forces, respectively. We employ log-conformation algorithm to solve High Weissenberg Non-linear problem (HWNP), the details and the validation of which can be referred to our previous paper⁴¹. Numerical model with its boundary conditions is presented in Fig. 7.

References

- Huang, L. R., Cox, E. C., Austin, R. H. & Sturm, J. C. Continuous particle separation through deterministic lateral displacement. *Sci.* **304**, 987 (2004).
- Inglis, D. W., Herman, N. & Vesey, G. Highly accurate deterministic lateral displacement device and its application to purification of fungal spores. *Biomicrofluidics* **4**, 1852 (2010).
- Inglis, D. W. *et al.* Microfluidic device for label-free measurement of platelet activation. *Lab on A Chip* **8**, 925–931 (2008).
- Ranjan, S., Zeming, K. K., Jureen, R., Fisher, D. & Zhang, Y. Dld pillar shape design for efficient separation of spherical and non-spherical bioparticles. *Lab on A Chip* **14**, 4250 (2014).
- Kwek, Z. K., Thoriq, S., Chen, C. H. & Zhang, Y. Asymmetrical deterministic lateral displacement gaps for dual functions of enhanced separation and throughput of red blood cells. *Sci. Reports* **6**, 22934 (2016).
- Karabacak, N. M. *et al.* Microfluidic, marker-free isolation of circulating tumor cells from blood samples. *Nat. Protoc.* **9**, 694–710 (2014).
- Loutherback, K. *et al.* Deterministic separation of cancer cells from blood at 10 ml/min. *Aip Adv.* **2**, 42107 (2012).
- Jiang, J. *et al.* An integrated microfluidic device for rapid and high-sensitivity analysis of circulating tumor cells. *Sci. Reports* **7**, 42612 (2017).

9. Inglis, D. W. Critical particle size for fractionation by deterministic lateral displacement. *Lab on A Chip* **6**, 655 (2006).
10. Davis, J. A. Microfluidic separation of blood components through deterministic lateral displacement. *Diss. & Theses - Gradworks* (2008).
11. Louterback, K., Puchalla, J., Austin, R. H. & Sturm, J. C. Deterministic microfluidic ratchet. *Phys. Rev. Lett.* **102**, 045301 (2009).
12. Holm, S., Beech, J., Barrett, M. & Tegenfeldt, J. Simplifying microfluidic separation devices towards field-detection of blood parasites. *Anal. Methods* **8**, 3291–3300 (2016).
13. Holm, S. H., Beech, J. P., Barrett, M. P. & Tegenfeldt, J. O. Separation of parasites from human blood using deterministic lateral displacement. *Lab on A Chip* **11**, 1326–1332 (2011).
14. D'Avino, G. Non-newtonian deterministic lateral displacement separator: theory and simulations. *Rheol. Acta* **52**, 221–236 (2013).
15. Beech, J. P. & Tegenfeldt, J. O. Tuneable separation in elastomeric microfluidics devices. *Lab on A Chip* **8**, 657 (2008).
16. Devendra, R., Drazer, G. & Chem, A. Gravity driven deterministic lateral displacement for particle separation in microfluidic devices. *Anal. Chem.* **84**, 10621–7 (2012).
17. Beech, J. P., Jönsson, P. & Tegenfeldt, J. O. Tipping the balance of deterministic lateral displacement devices using dielectrophoresis. *Lab on A Chip* **9**, 2698 (2009).
18. Bogunovic, L., Eichhorn, R., Regtmeier, J., Anselmetti, D. & Reimann, P. Particle sorting by a structured microfluidic ratchet device with tunable selectivity: Theory and experiment. *Soft Matter* **8**, 3900–3907 (2012).
19. Collins, D. J., Alan, T. & Neild, A. Particle separation using virtual deterministic lateral displacement (vdld). *Lab on A Chip* **14**, 1595–603 (2014).
20. Yuan, D. *et al.* On-chip microparticle and cell washing using coflow of viscoelastic fluid and newtonian fluid. *Anal. Chem.* **89**, 9574–9582, <https://doi.org/10.1021/acs.analchem.7b02671> (2017).
21. Yuan, D. *et al.* Continuous plasma extraction under viscoelastic fluid in a straight channel with asymmetrical expansion-contraction cavity arrays. *Lab Chip* **16**, 3919–3928 (2016).
22. Liu, C. *et al.* Sheathless focusing and separation of diverse nanoparticles in viscoelastic solutions with minimized shear thinning. *Anal. Chem.* **88**, 12547–12553, <https://doi.org/10.1021/acs.analchem.6b04564> (2016).
23. Liu, C. *et al.* Size-based separation of particles and cells utilizing viscoelastic effects in straight microchannels. *Anal. Chem.* **87**, 6041–6048, <https://doi.org/10.1021/acs.analchem.5b00516> (2015).
24. Tian, F. *et al.* Microfluidic co-flow of newtonian and viscoelastic fluids for high-resolution separation of microparticles. *Lab Chip* **17**, 3078–3085 (2017).
25. Del Giudice, F. *et al.* Particle alignment in a viscoelastic liquid flowing in a square-shaped microchannel. *Lab Chip* **13**, 4263–4271 (2013).
26. Villone, M., D'Avino, G., Hulsen, M., Greco, F. & Maffettone, P. Particle motion in square channel flow of a viscoelastic liquid: Migration vs. secondary flows. *J. Non-Newtonian Fluid Mech.* **195**, 1–8 (2013).
27. Del Giudice, F. *et al.* Magnetophoresis 'meets' viscoelasticity: deterministic separation of magnetic particles in a modular microfluidic device. *Lab Chip* **15**, 1912–1922 (2015).
28. Zhang, J. *et al.* A novel viscoelastic-based ferrofluid for continuous sheathless microfluidic separation of nonmagnetic microparticles. *Lab Chip* **16**, 3947–3956 (2016).
29. Xiang, N. *et al.* Fundamentals of elasto-inertial particle focusing in curved microfluidic channels. *Lab Chip* **16**, 2626–2635 (2016).
30. Ho, B. P. & Leal, L. G. Migration of rigid spheres in a two-dimensional unidirectional shear flow of a second-order fluid. *J. Fluid Mech.* **76**, 783–799 (1976).
31. Li, G., Mckinley, G. & Ardekani, A. Dynamics of particle migration in a channel flow of viscoelastic fluids. *J. Fluid Mech.* **785**, 486–505 (2015).
32. Seo, K. W., Yang, J. K. & Sang, J. L. Lateral migration and focusing of microspheres in a microchannel flow of viscoelastic fluids. *Phys. Fluids* **26**, 209–210 (2014).
33. Leshansky, A. M., Bransky, A., Korin, N. & Dinnar, U. Tunable nonlinear viscoelastic “focusing” in a microfluidic device. *Phys. Rev. Lett.* **98**, 234501 (2007).
34. D'Avino, G. *et al.* Single line particle focusing induced by viscoelasticity of the suspending liquid: theory, experiments and simulations to design a micropipe flow-focuser. *Lab Chip* **12**, 1638–1645 (2012).
35. Bird, R. B. *Dynamics of polymeric liquids* (Wiley, 1987).
36. Joseph, D. D., Liu, Y. J., Poletto, M. & Feng, J. Aggregation and dispersion of spheres falling in viscoelastic liquids. *J. Non-Newtonian Fluid Mech.* **54**, 45–86 (1994).
37. Kulrattanarak, T., Sman, R. G. M. V. D., Schroën, C. G. P. H. & Boom, R. M. Analysis of mixed motion in deterministic ratchets via experiment and particle simulation. *Microfluid. & Nanofluidics* **10**, 843–853 (2011).
38. Beech, J. *Microfluidics Separation and Analysis of Biological Particles* (Lund University, 2011).
39. James, D. F. Boger fluids. *Annu. Rev. Fluid Mech.* **41**, 129–142 (2009).
40. Li, Y. K. *et al.* Numerical study on secondary flows of viscoelastic fluids in straight ducts: Origin analysis and parametric effects. *Comput. & Fluids* **152**, 57–73 (2017).
41. Li, D. Y. *et al.* Efficient heat transfer enhancement by elastic turbulence with polymer solution in a curved microchannel. *Microfluid. & Nanofluidics* **21**, 10 (2017).
42. Balvin, M., Sohn, E., Iracki, T., Drazer, G. & Frechette, J. Directional locking and the role of irreversible interactions in deterministic hydrodynamics separations in microfluidic devices. *Phys. Rev. Lett.* **103**, 078301 (2009).
43. Jasak, H. Error analysis and estimation for the finite volume method with applications to fluid flows. *Imp. Coll. Lond.* **m**, A385 (1996).

Acknowledgements

The authors would like to acknowledge the financial support for this project from the National Natural Science Foundation of China (51606054, 51776057), China Postdoctoral Science Foundation (2013M541374), Postdoctoral Scientific Research Development Fund (LBH-Q16087), Heilongjiang Province Postdoctoral Foundation (LBH-Z15063), and China Postdoctoral International Exchange Program. They are also very grateful for the enthusiastic help of all members of the Complex Flow and Heat Transfer Laboratory of Harbin Institute of Technology.

Author Contributions

Y.K.L., Y.Y.L., X.B.L., and F.C.L. conceived the experiments; Y.K.L. conducted the experiments and analysed the results; Y.K.L. and H.N.Z. did the numerical simulations; Y.K.L., H.N.Z., J.W. and S.Z.Q. drafted the main manuscript. All authors reviewed the manuscript.

Additional Information

Supplementary information accompanies this paper at <https://doi.org/10.1038/s41598-018-21827-7>.

Competing Interests: The authors declare no competing interests.

Publisher's note: Springer Nature remains neutral with regard to jurisdictional claims in published maps and institutional affiliations.



Open Access This article is licensed under a Creative Commons Attribution 4.0 International License, which permits use, sharing, adaptation, distribution and reproduction in any medium or format, as long as you give appropriate credit to the original author(s) and the source, provide a link to the Creative Commons license, and indicate if changes were made. The images or other third party material in this article are included in the article's Creative Commons license, unless indicated otherwise in a credit line to the material. If material is not included in the article's Creative Commons license and your intended use is not permitted by statutory regulation or exceeds the permitted use, you will need to obtain permission directly from the copyright holder. To view a copy of this license, visit <http://creativecommons.org/licenses/by/4.0/>.

© The Author(s) 2018